JACS
JOURNAL OF THE AMERICAN CHEMICAL SOCIETY

Article

Mediator–Template Assembly of Nanoparticles

Mathew M. Maye, I-Im S. Lim, Jin Luo, Zia Rab, Daniel Rabinovich, Tianbo Liu, and Chuan-Jian Zhong

J. Am. Chem. Soc., **2005**, 127 (5), 1519-1529• DOI: 10.1021/ja044408y • Publication Date (Web): 11 January 2005

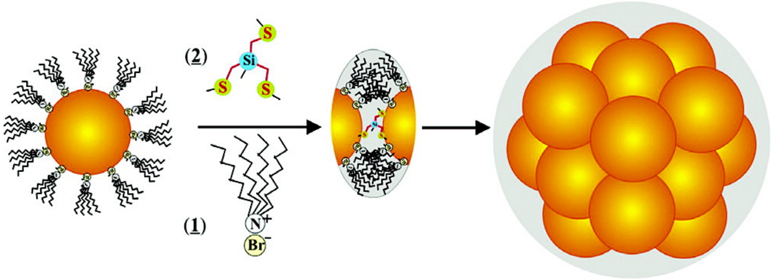

ACS Publications
High quality. High impact.

Journal of the American Chemical Society is published by the American Chemical Society. 1155 Sixteenth Street N.W., Washington, DC 20036

J|A|C|S
ARTICLES

Mediator−Template Assembly of Nanoparticles

Mathew M. Maye, I-Im S. Lim, Jin Luo, Zia Rab, Daniel Rabinovich,[†]
Tianbo Liu,[‡] and Chuan-Jian Zhong*

*Contribution from the Department of Chemistry, State University of New York at Binghamton,
Binghamton, New York 13902, Department of Chemistry, The University of North Carolina at
Charlotte, Charlotte, North Carolina 28223, and Department of Chemistry, Lehigh University,
Bethlehem, Pennsylvania 18015*

Received September 14, 2004; E-mail: cjzhong@binghamton.edu

Abstract: The ability to construct size- and shape-controllable architectures using nanoparticles as building blocks is essential for the exploration of nanoparticle-structured properties. This paper reports findings of an investigation of a mediator−template strategy for the size-controllable assembly of nanoparticles. This strategy explores multidentate thioether ligands as molecular mediators and tetraalkylammonium-capped gold nanoparticles (5 nm) as templates toward the preparation of size-controllable and monodispersed spherical assemblies (∼20−300-nm diameters). The combination of the mediation force of the multidentate thioether and the hydrophobic force of the tetraalkylammonium template establishes the interparticle linkage and stability. The morphological properties of the spherical assemblies have been characterized using TEM, AFM, and SAXS techniques. The finding of the soft−hard nature of the nanoparticle assemblies and their interactions with contacting substrates could form the basis of a new strategy for manipulating nanoscale linkages between nanoparticle assemblies, soldering nanoelectronics, and constructing nanosensor devices. The intriguing light scattering and optical absorption properties in response to assembly, disassembly, sizing, and interparticle spacing parameters have been characterized by dynamic light scattering and spectrophotometric measurements. The discovery of the controlled disassembly into individual nanoparticles and the size regulation by a third capping component could form the basis for applications in controlled drug delivery. The fundamental basis for the mediator−template strategy as a versatile assembly technique is further discussed in terms of experimental and theoretical correlations of the morphological and optical properties.

Introduction

Many areas of nanotechnology involve the use of nanoparticle-based materials in applications such as sensors, catalysis, and information storage. These applications require the ability to assemble nanoparticles into an ensemble with controllable size, shape, and interparticle spatial properties so that the unique nanoscale properties can be effectively exploited.[1] The abilities to synthesize nanoparticles and to assemble nanoparticles in controllable sizes and shapes are therefore increasingly important.[2] Many existing approaches have explored place-exchanging,[3] stepwise assembling,[4−7] DNA linking,[8−10] hydrogen bonding,[11,12] polymer-based molecular recognition,[13] or multidentate thioethers[14,15] to mediate the assembly of nanoparticles. While a variety of assembly methods have been demonstrated,

---

[†] The University of North Carolina at Charlotte.

[‡] Lehigh University.

(1) (a) Daniel, M.-C.; Astruc, D. *Chem. Rev.* **2004**, *104*, 293−346. (b) Zhong, C. J.; Maye, M. M. *Adv. Mater.* **2001**, *13*, 1507−1511.

(2) (a) Sau, T. K.; Murphy, C. J. *J. Am. Chem. Soc.* **2004**, *126*, 8648−8649. (b) Wei, Z. Q.; Mieszawska, A. J.; Zamborini, F. P. *Langmuir* **2004**, *20*, 4322−4326. (c) Chen, S. *Langmuir* **2001**, *17*, 6664−6668. (d) Milliron, D. J.; Hughes, S. M.; Cui, Y.; Manna, L.; Li, J. B.; Wang, L. W.; Alivisatos A. P. *Nature* **2004**, *430*, 190−195. (e) Puntes, V. F.; Zanchet, D.; Erdonmez, C. K.; Alivisatos, A. P. *J. Am. Chem. Soc.* **2002**, *124*, 12874−12880. (f) Kim, F.; Connor, S.; Song, H.; Kuykendall, T.; Yang, P. *Angew. Chem., Int. Ed.* **2004**, *43*, 3673−3677. (g) Thomas, K. G.; Barazzouk, S.; Ipe, B. I.; Joseph, S. T. S.; Kamat, P. V. *J. Phys. Chem. B* **2004**, *108*, 13066−13068.

(3) Templeton, A. C.; Wuelfing, W. P.; Murray, R. W. *Acc. Chem. Res.* **2000**, *33*, 27−36.

(4) Andres, R. P.; Bielefeld, J. D.; Henderson, J. I.; Janes, D. B.; Kolagunta, V. R.; Kubiak, C. P.; Mahoney, W. J.; Osifchin, R. G. *Science* **1996**, *273*, 1690−1693.

(5) Freeman, R. G.; Garbar, K. C.; Allison, K. J.; Bright, R. M.; Davis, J. A.; Guthrie, A. P.; Hommer, M. B.; Jackson, M. A.; Smith, P. C.; Walter, D. G.; Natan, M. J. *Science* **1995**, *267*, 1629−1632.

(6) Zamborini, F. P.; Hicks, J. F.; Murray, R. W. *J. Am. Chem. Soc.* **2000**, *122*, 4514−4515.

(7) (a) Brust, M.; Bethell, D.; Kiely, C. J.; Schiffrin, D. J. *Langmuir* **1998**, *14*, 5425−5429. (b) Bethell, D.; Brust, M.; Schiffrin, D. J.; Kiely, C. J. *J. Electroanal. Chem.* **1996**, *409*, 137−143. (c) Brust, M.; Kiely, C. J.; Bethell, D.; Schiffrin, D. J. *J. Am. Chem. Soc.* **1998**, *120*, 12367−12368. (d) Baum, T.; Bethell, D.; Brust, M.; Schiffrin, D. J. *Langmuir* **1985**, *15*, 866−871.

(8) (a) Mirkin, C. A.; Letsinger, R. L.; Mucic, R. C.; Storhoff. J. J. *Nature* **1996**, *382*, 607−609. (b) Elghanian, R.; Storhoff, J. J.; Mucic, R. C.; Letsinger, R. L.; Mirkin, C. A. *Science* **1997**, *277*, 1078−1081. (c) Taton, T. A.; Mucic, R. C.; Mirkin, C. A.; Letsinger, R. L. *J. Am. Chem. Soc.* **2000**, *122*, 6305−6306. (d) Wang, G.; Murray, R. W. *Nano Lett.* **2004**, *4*, 95−101.

(9) Alivisatos, A. P.; Johnsson, K. P.; Peng, X. G.; Wilson, T. E.; Loweth, C. J.; Bruchez, M. P.; Schultz, P. G. *Nature* **1996**, *382*, 609−611.

(10) Mbindyo, J. K. N.; Reiss, B. D.; Martin, B. R.; Keating, C. D.; Natan, M. J.; Mallouk, T. E. *Adv. Mater.* **2001**, *13*, 249−254.

(11) Zheng, W. X.; Maye, M. M.; Leibowitz, F. L.; Zhong, C. J. *Anal. Chem.* **2000**, *72*, 2190−2199.

(12) Boal, A. K.; Rotello, V. M. *J. Am. Chem. Soc.* **2000**, *122*, 734−735.

(13) (a) Boal, A. K.; Ilhan, F.; DeRouchey, J. E.; Thurn-Albrecht, T.; Russell T. P.; Rotello, V. M. *Nature* **2000**, *404*, 746−748. (b) Boal, A. K.; Rotello, V. M. *J. Am. Chem. Soc.* **2002**, *124*, 5019−5024.

(14) Maye, M. M.; Chun, S. C.; Han, L.; Rabinovich, D.; Zhong, C. J. *J. Am. Chem. Soc.* **2002**, *124*, 4958−4959.

10.1021/ja044408y CCC: $30.25 © 2005 American Chemical Society

Scheme 1. Schematic Illustrations of the Mediation−Template Strategy for **2**-Mediated Assembly of **1**-Capped Gold Nanoparticles (**1**/Au)

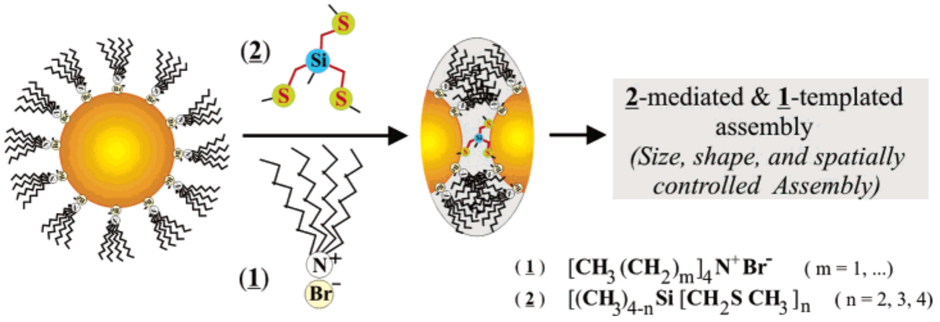

the ability to precisely control size, shape, and interparticle spatial properties is rarely reported because of the lack of molecular-level understanding of the interparticle interactions and reactivities.

We have recently demonstrated molecularly mediated thin film assemblies[11,16] and multidentate thioether-mediated spherical assemblies of monolayer-capped nanoparticles.[14,15] The molecular mediation involved hydrogen bonding or covalent bonding in the thin film assembly case and coordination bonding in the spherical assembly case. The key element in our approach is a mediator−template strategy for the assembly of nanoparticles. The understanding of molecular driving forces exerted by molecular linkers or multidentate thioethers as mediators and monolayer- or surfactant-capping molecules as templating agents could lead to a general assembly strategy toward abilities in size, shape, and spatial control. Consider, for example, a system in which multidentate thioethers, $Me_{4-n}Si(CH_2SMe)_n$ (**2**), are used as mediators and tetraalkylammonium bromides, $[CH_3(CH_2)_m]_4N^+Br^-$ (**1**), as templating agents. Scheme 1 illustrates the general concept of the **2**-mediated assembly of **1**-capped gold nanoparticles (**1**/Au), which involves the interparticle linkage by a combination of bridging (**2**) and templating (**1**).

Using this mediator−template strategy for the assembly of **1**-capped gold nanoparticles via multidentate thioether mediators (e.g., tetra[(methylthio)methyl]silane, $Si(CH_2SCH_3)_4$, and methyltris[(methylthio)methyl]silane, $MeSi(CH_2SCH_3)_3$),[14,15] our initial findings revealed the formation of nanoparticle assemblies with spherical shape and controllable size. It is interesting that the spherical shaping nature resembles other assemblies of nanoparticles derived from different strategies such as the use of polymer- or dendrimer-based molecular recognition ligands.[13−15,17−18] In contrast, our approach using thioether-based ligands is grounded in the basic thioether−gold coordination chemistry,[14,15] which has been documented in other reports of the preparation of gold nanoparticles capped with monodentate dialkyl thioethers and terminal-functionalized thioether.[19] The finding of the size-controllable spherical assemblies of nanoparticles mediated by multidentate thioether ligands has little or no precedent. This mediator−template combination is simple and effective. The mediation force exploits the coordination reactivity of **2** to Au, which can be manipulated by the number of thioether groups on **2**, whereas the templating force exerted by the surfactant reactivity of **1** generates geometric effect to the assembly, which is dependent on its chain length and structure. The fundamental basis of our mediator−template assembly strategy may be related to the well-documented surfactant-based micelle theory,[20] in which the assembly of surfactants could form ensembles with different sizes and shapes depending on its chain length and concentration. The surfactant-based micelle theory predicts that spheres usually prevail when the relative geometric ratio (R) of surfactant versus packing structure,

$$R = \upsilon/\alpha_0 l$$

is below a critical value, where υ is the volume of the surfactant molecule, α_0 the optimum surface area per surfactant, and l the length of the surfactant molecule. $R < {}^1/_3$ favors spherical aggregates, whereas $R > {}^1/_2$ favors cylindrical aggregates. The investigation of whether this theoretical basis applies to our mediator−template assembly of nanoparticles should be very interesting for developing abilities in controlling size, shape, and interparticle spatial properties.

One potential application of the nanoparticle-structured assembly is the development of sensing array, drug delivery, or information storage materials in chemical/biological environments via electronic, optical, and magnetic signaling transducers. The nanostructure sequesters chemical or biological molecules into the interior or surface with spongelike access or specific binding properties, which could alter and modify the electrical or optical properties of the nanoscale materials.[21,22] This type of nanostructured properties is a result of the predominance of interfacial phenomena at the nanoscale dimension, which have been documented by excellent examples[1] showing the importance of size, shape, and interparticle spatial properties. In this report, we will show results of systematic characteriza-

---

(15) Maye, M. M.; Luo, J.; Lim, I.-I. S.; Han, L.; Kariuki, N. N.; Rabinovich, D.; Liu, T.; Zhong, C. J. *J. Am. Chem. Soc.* **2003**, *125*, 9906−9907.

(16) (a) Leibowitz, F. L.; Zheng, W. X.; Maye, M. M.; Zhong, C. J. *Anal. Chem.* **1999,** *71*, 5076−5083. (b) Han, L.; Luo, J.; Kariuki, N. N.; Maye, M. M.; Jones, V. W.; Zhong, C. J. *Chem. Mater.* **2003**, *15*, 29−37. (c) Han, L.; Maye, M. M.; Leibowitz, F. L.; Ly, N. K.; Zhong, C. J. *J. Mater. Chem.* **2001**, *11*, 1259−1264. (d) Maye, M. M.; Luo, J.; Han, L.; Zhong, C. J. *Nano Lett.* **2001**, *1*, 575−580. (e) Han, L.; Wu, W.; Kirk, F. L.; Luo, J.; Maye, M. M.; Kariuki, N. N.; Lin, Y.; Wang, C.; Zhong, C. J. *Langmuir* **2004**, *14*, 6019−6025.

(17) (a) Frankamp, B. L.; Boal, A. K.; Rotello, V. M. *J. Am. Chem. Soc.* **2002**, *124*, 15146−15147. (b) Frankamp, B. L.; Uzun, O.; Ilhan, F.; Boal, A. K.; Rotello, V. M. *J. Am. Chem. Soc.* **2002**, *124*, 892−893. (c) Carroll, J. B.; Frankamp, B. L.; Srivastava, S.; Rotello, V. M. *J. Mater. Chem.* **2004**, *14*, 690−694.

(18) Kariuki, N. N.; Han, L.; Ly, N. K.; Peterson, M. J.; Maye, M. M.; Liu, G.; Zhong, C. J. *Langmuir* **2002**, *18*, 8255−8259.

(19) (a) Li, X. M.; de Jong, M. R.; Inoue, K.; Shinkai, S.; Huskens, J.; Reinhoudt, D. N. *J. Mater. Chem.* **2001**, *11*, 1919−1923. (b) Pankau, W. M.; Verbist, K.; Kiedrowski, G. *Chem. Commun.* **2001**, 519−520.

(20) Israelachvilli, J. N.; Mitchell, D. J.; Ninham, B. W. *J. Chem. Soc., Faraday Trans 2* **1976**, *72*, 1525−1568.

(21) Han, L.; Daniel, D. R.; Maye, M. M.; Zhong, C. J. *Anal. Chem.* **2001**, *73*, 4441−4449.

(22) Zamborini, F. P.; Leopold, M. C.; Hicks, J. F.; Kulesza, P. J.; Malik, M. A.; Murray, R. W. *J. Am. Chem. Soc.* **2002**, *124*, 8958−8964.

tions of the mediator−template assembly of nanoparticles toward size-controllable nanostructures. We will also describe interesting morphological and optical properties of the nanoparticle assemblies which could potentially be exploited for optical sensing applications.

Experimental Section

Chemicals. Hydrogen tetracholoroaurate ($HAuCl_4$, 99%), tetraoctylammonium bromide (**1**, 99%), decanethiol (**3**, 96%), sodium borohydride ($NaBH_4$, 99%), toluene (Tl, 99.8%), hexane (Hx, 99.9%), and ethanol (EtOH, 99.9%) were purchased from Aldrich and used as received. Water was purified with a Millipore Milli-Q water system.

Multidentate thioethers (**2**) were synthesized in the laboratory.[23] The tridentate thioether $MeSi(CH_2SMe)_3$ (TE_3) was synthesized as described in the literature, and the tetrathioether $Si(CH_2SMe)_4$ (TE_4) was prepared similarly, starting from $SiCl_4$ and $LiCH_2SMe$.[23] The coordination chemistry of **2** toward various transition-metal ions has been investigated.[23,24] Unless otherwise noted, most examples reported in this work involved the use of TE_3 as the **2**-mediator.

Synthesis of Gold Nanoparticles. Gold nanoparticles capped with tetraoctylammonium bromide (**1**) monolayer shells were synthesized according to the two-phase protocol.[25] In a typical synthesis, tetraoctylammonium bromide (0.55 g) was used as a phase-transfer reagent and was dissolved to 32 mL of toluene (31 mM). After stirring for 15 min, an aqueous solution (20 mL) of $HAuCl_4$ (0.077 g, 9.5 mM) was added under stirring. The $AuCl_4^-$ ions were completely transferred from the aqueous solution to toluene within 15 min. After stirring for 30 min, the organic phase was separated, and the aqueous phase was discarded. With the remaining toluene solution, a 5-fold excess of aqueous reducing agent, $NaBH_4$, was added dropwise into the solution under stirring. The solution turned from orange-red to a deep red color. The reaction was then allowed to continue under stirring at room temperature for 24 h. The aqueous phase was removed and the Tl solution was treated with drying agent to remove trace water. The resulting Tl solution contained **1**-capped gold nanoparticles (**1**/Au) as well as excess **1** (~31 mM). Using this method, we have obtained Au nanoparticles with core sizes ranging from 4.8 to 6.4 nm and standard deviations in the range of ±0.5−1.0 nm.

Assembly of Nanoparticles. The assembly of mediators (**2**) and nanoparticles (**1**/Au) were carried out under controlled conditions depending on the specific measurement or characterization. For example, in using the UV−visible method to monitor the reaction, a quartz cuvette with a path length of 1 cm was used as the reaction vessel. Initial concentrations of gold nanoparticles were determined from the absorbance and were estimated using the average diameter of the particles. A molar absorptivity (ϵ_{Au}) of 1.1×10^7 $M^{-1} \cdot cm^{-1}$ was used for **1**/Au of ~5-nm core diameter.[26] Diluted solutions of **1**/Au in toluene were utilized (~0.1 μM). An aliquot of a stock solution of 500 μM of **2** in toluene was quantitatively added into the nanoparticle solution using a micropipet. The solution was quickly homogenized by purging (for ~2 s) before the measurement. Similar preparation procedures were used for other measurements or characterizations, but the actual experimental conditions varied slightly in terms of the average size and concentration of the nanoparticles and the structure and concentration of the mediators.

Instrumentation. UV−visible (UV−vis) spectra were acquired with an HP 8453 spectrophotometer. The spectra were collected over the range of 200−1100 nm.

Transmission electron microscopy (TEM) was performed on Hitachi H-7000 Microscope (100 kV). TEM samples were taken from the reaction solutions and diluted ~1:10 in toluene. The solution was then drop cast onto carbon-coated Cu grids and dried in less than 1 min.

Dynamic light scattering (DLS) experiments were carried out using a commercial Brookhaven Instrument Inc. laser light scattering spectrometer equipped with a solid-state laser operating at 532 nm. The detailed descriptions on the instrumentation have been reported elsewhere.[27] The **1**/Au concentrations used were a tenth of the concentration used for spectrophotometric measurement, with the **2** to **1**/Au ratios remaining similar. DLS measures the intensity−intensity time correlation function $G^{(2)}(\Gamma)$ by means of a BI-9000 AT multichannel digital correlator: $G^{(2)}(\Gamma) = A(1 + b|g^{(1)}(\tau)|^2)$ where A, b, and $|g^{(1)}(\tau)|$ are, respectively, the background, a coherence factor, and the normalized electric field time correlation function. The field correlation function $|g^{(1)}(\tau)|$ was analyzed by the constrained regularized CONTIN method[27] to yield information on the distribution of the characteristic line width (Γ) from $|g^{(1)}(\tau)| = \int G(\Gamma)e^{-\Gamma\tau}d\Gamma$. The normalized distribution function of the characteristic line width, $G(\Gamma)$, so obtained can be used to determine an average apparent translational diffusion coefficient D_{app}: $D_{app} = \Gamma/q^2$. The hydrodynamic radius R_h is related to D via the Stokes−Einstein equation: $R_h = kT/(6\pi\eta D)$ where k is the Boltzmann constant and η is the viscosity of the solvent at temperature T. From DLS measurements, we can obtain the particle-size distribution in solution from a plot of $\Gamma G(\Gamma)$ versus R_h.

Small-angle X-ray scattering (SAXS) experiments were performed at the X10A Exxon Beam Line, National Synchrotron Light Source (NSLS) at Brookhaven National Laboratory (BNL). The incident beam wavelength (λ) was tuned at 1.1 Å. A MAR CCD detector was used as the detection system. Samples were introduced into glass capillaries with a 2-mm diameter at room temperature. The concentrations of nanoparticles were ~10× of those used for the spectrophotometric measurements.

A Multimode NanoScope IIIa (Digital Instruments), equipped with an E scanner (maximum scan size: 16 μm), was utilized for atomic force microscopic (AFM) imaging. The capability of TappingMode (TM) AFM allows imaging at minimum disruption of the nanostructures. Standard silicon tapping cantilevers (Nanosensors) were used with a force constant of 40 N/m (TESP). The probe has nominal tip radius of curvature of ~10 nm. The instrument was calibrated by imaging standard calibration gratings. All images were acquired in tapping mode. Solution samples of the nanoparticle assemblies were cast onto freshly cleaved mica or freshly cleaved HOPG (highly ordered pyrolytic graphite) sheets, followed by solvent evaporation at ambient condition.

X-ray photoelectron spectroscopy (XPS) measurements were made using a Physical Electronics Quantum 2000 Scanning ESCA Microprobe. Monochromatic Al Kα X-rays (1486.7 eV) were used as source for excitation. The percentages of individual elements were determined from the relative composition analysis of the peak areas of the bands.

Results and Discussion

The description and discussion of our results are divided into two sections. In the first section, we describe the formation and morphological properties of spherical assemblies derived from the mediator−template assembly of **1**/Au. The morphological

---

(23) (a) Yim, H. W.; Tran, L. M.; Dobbin, E. D.; Rabinovich, D.; Liable-Sands, L. M.; Incarvito, C. D.; Lam, K.-C.; Rheingold, A. L. *Inorg. Chem.* **1999**, *38*, 2211−2215. (b) Yim, H. W.; Lam. K.-C.; Rheingold, A. L.; Rabinovich, D. *Polyhedron* **2000**, *19*, 849−853.

(24) (a) Yin, H. W.; Tran, L. M.; Dobbin, E. D.; Rabinovich, D. Liable-Sands, L. M.; Concolino, T. E.; Rheingold, A. L. *Inorg. Chem*. **1999**, *38*, 6234−6239. (b) Yim, H. W.; Rabinovich, D.; Lam, K.-C.; Golen, J. A.; Rheingold, A. L. *Acta Crystallogr.* **2003**, *E59*, m556−m558.

(25) (a) Brust, M.; Walker, M.; Bethell, D.; Schiffrin, D. J.; Whyman, R. *J. Chem. Soc., Chem. Commun.* **1994**, 801−802. (b) Fink, J.; Kiely, C. J.; Bethell, D.; Schiffrin, D. J. *Chem. Mater*. **1998**, *10*, 922−926. (c) Hostetler, M. J.; Wingate, J. E.; Zhong, C. J.; Harris, J. E.; Vachet, R. W.; Clark, M. R.; Londono, J. D.; Green, S. J.; Stokes, J. J.; Wignall, G. D.; Glish, G. L.; Porter, M. D.; Evans, N. D.; Murray, R. W. *Langmuir* **1998**, *14*, 17−30. (d) Maye, M. M.; Zheng, W. X.; Leibowitz, F. L.; Ly, N. K.; Zhong, C. J. *Langmuir* **2000**, *16*, 490−497. (e) Maye, M. M.; Zhong, C. J. *J. Mater. Chem.* **2000**, *10*, 1895−1901. (f) Thomas, K. G.; Zajicek, J.; Kamat, P. V. *Langmuir* **2002**, *18*, 3722−3727. (g) Saunders, A. E.; Sigman, M. B.; Korgel, B. A. *J. Phys. Chem. B* **2004**, *108*, 193−199.

(26) Maye, M. M.; Han, L.; Kariuki, N. N.; Ly, N. K., Chan, W.-B.; Luo, J.; Zhong, C. J. *Anal. Chim. Acta* **2003**, *496*, 17−27.

(27) Liu, T. *J. Am. Chem. Soc.* **2002**, *124*, 10942−10943.

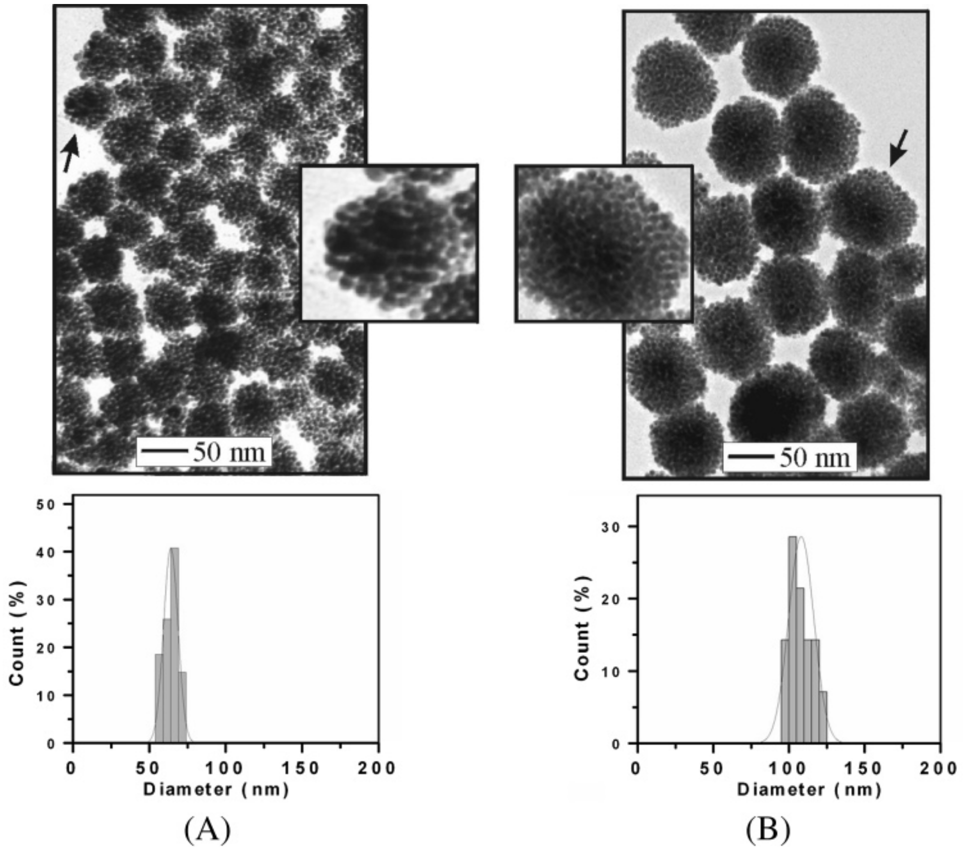

Figure 1. TEM micrographs showing the **2**-mediated assemblies of **1**/Au obtained from two different ratios, (A) $r \approx 660$ ([**1**/Au] = 0.1 μM, [**2**] = 66 μM), and (B) $r \approx 200$ ([**1**/Au] = 0.1 μM, [**2**] = 20 μM). Insets: enlarged views of the indicated assemblies. The corresponding size distributions, 64 ± 14 nm (A) and 104 ± 18 nm (B), are based on 30 counts of the assemblies in each case. (**1**/Au = 5.1 ± 0.9 nm).

properties were characterized using TEM, AFM, and SAXS techniques. In the second section, we focus on the assessment of the optical properties of the nanoparticle assemblies in response to processes such as assembly and disassembly and parameters such as size and interparticle spatial properties. The optical properties were characterized by measurements of dynamic light scattering and surface plasmon resonance absorption.

1. Morphological Properties. One of the unique properties for the multidentate thioether-mediated assembly of **1**-capped gold nanoparticles is the formation of spherical assemblies of the nanoparticles in solutions.[14,15] The size and monodispersity of such spherical assemblies can be fine-tuned by a combination of structural and experimental parameters and have been characterized by an array of techniques, including TEM, AFM, and SAXS, which are detailed in the following subsections.

1.1 TEM. When a mediator agent (**2**) was added into a toluene solution of **1**/Au, the solution displayed a gradual color change from red to purple. Accompanying the change in optical properties, which will be detailed in a later section, nanoparticle assemblies with intriguing morphological properties were revealed by TEM characterization of samples from the solution. Figure 1 shows a representative set of TEM micrographs for **2**-mediated **1**/Au assemblies, which were sampled from two assembling solutions with different **2** to **1**/Au concentration ratios ([**2**]/[**1**/Au] = r), that is, 660 (A) and 200 (B).

The combination of **1** and **2** led to the formation of spherical assemblies of **1**/Au with relatively high monodispersity. The average diameters of the assemblies are dependent on r, as shown by the determined diameters of 64 ± 14 nm for $r \approx 660$ and 104 ± 18 nm for $r \approx 200$. The initial nanoparticle assemblies were soluble, as evidenced by the fact that the blue or purple color of the solution was stable for a period of 1−5 h to 5−10 days before precipitation occurred, depending on the size of the nanoparticle assemblies. For example, a solution of ~200-nm-sized assemblies prepared at a low r (1−10) precipitated from solution in ~2 h. In contrast, a solution of 80-nm-sized assemblies prepared from a high r (~500) stayed in the solution for ~3 days. In addition to size effect, the solubility is associated with the hydrophobic interactions between the solvent (Tl) and the surface organic layer of the nanoparticle assemblies. The assemblies also showed reversible precipitation−redispersion propensity. For example, larger assemblies could be redispersed in Tl solution for hours, whereas smaller assemblies could be easily redispersed for days. The multiple precipitation−redispersion cycles also allowed us to remove excess reactants or byproducts introduced into the nanoparticle or assembling solution. The cleaned nanoparticle assemblies were also stable in solutions, though they tended to precipitate faster than before cleaning. Figure 2 shows a representative TEM micrograph for a sample obtained after cleaning treatment (1×) of the assembly solution ($r = 10$). The spherical assemblies display remarkably high monodispersity with an average diameter of 212 ± 9 nm. Ordered domains and interconnected necklacelike morphologies

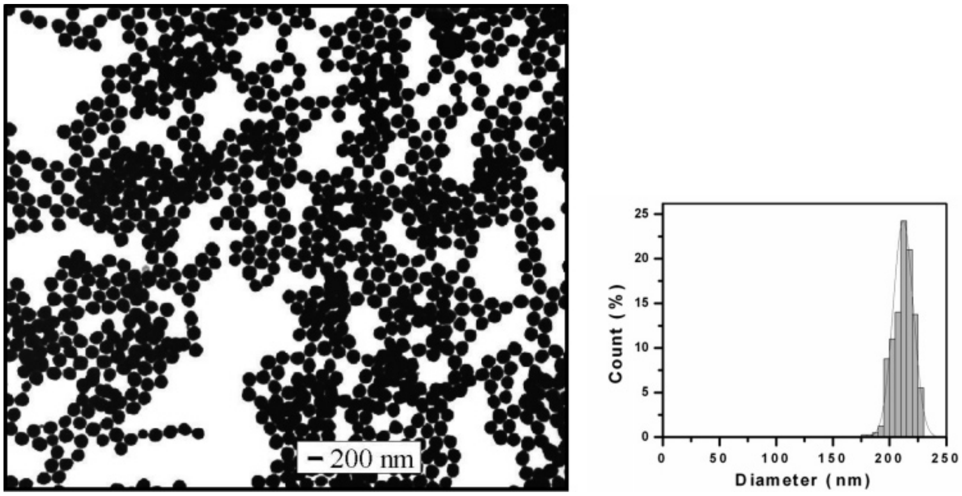

Figure 2. TEM micrograph for a sample obtained after cleaning treatment (1×) of the **2**-mediated assemblies of **1**/Au ($r = 10$). The corresponding size distribution (212 ± 9 nm) is based on 400 counts of the assemblies. (**1**/Au =5.3 ± 1.0 nm).

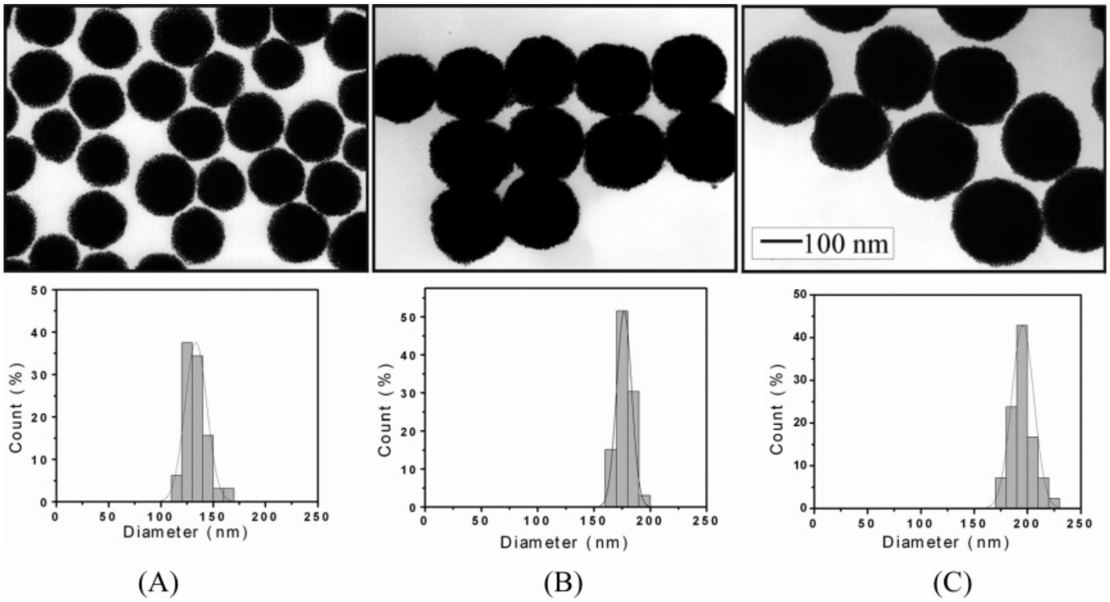

Figure 3. TEM micrographs for samples obtained from solutions of **2**-mediated assemblies of **1**/Au ($r = 100$ (A), 25 (B), and 10 (C)) after 1× cleaning treatment. Each micrograph has the same scale bar. The corresponding size distributions, 133 ± 10 nm (A), 176 ± 7 nm (B), and 195 ± 11 nm (C), are based on 30 counts of the assemblies in each case. (**1**/Au = 5.3 ± 1.0 nm).

can also be identified in the TEM image for these spherical assemblies.

Figure 3 shows a representative TEM micrograph for **2**-mediated **1**/Au assemblies derived from three additional *r* values (100 (A), 25 (B), and 10 (C)). These three samples showed similar spherical assemblies with diameters of 133 ± 10 (A), 176 ± 7 (B), and 195 ± 11 (C) nm.

A close examination of these assemblies reveals additional details about the morphologies. Figure 4 compares TEM micrographs for the nanoparticle assemblies before and after the precipitation−redispersion cycle. It is evident that the removal of the excess **1** and other reagents did not destabilize the spherical assemblies. In contrast, the spherical assemblies appeared more monodispersed and the nanoparticles seemed to be more densely packed. The precipitation−redispersion cycle led to an apparent increase of ∼10% in average size with a more dense packing feature. In comparison with the average size (164 nm) and size distribution (±12 nm) for the same nanoparticle assemblies before the cleaning treatment (e.g., $r \approx 25$) (Figure 4A), the spherical assemblies display an increased size (176 nm) and a higher monodispersity (±7 nm) (Figure 4B).

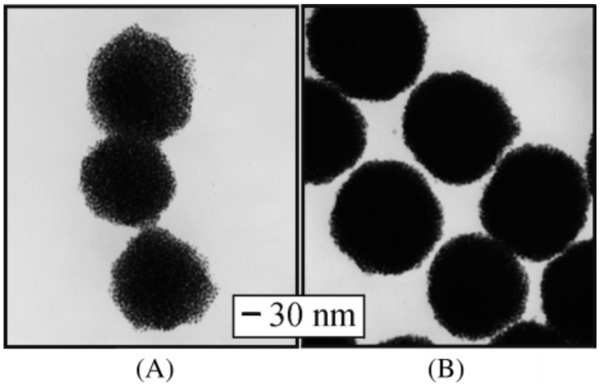

Figure 4. TEM micrographs comparing **2**-mediated assemblies of **1**/Au ($r = 25$) before (A) and after (B) precipitation−dispersion cycles (two times). Size distributions: 166 ± 12 (A) and 176 ± 7 (B) nm. (**1**/Au = 5.3 ± 1.0 nm).

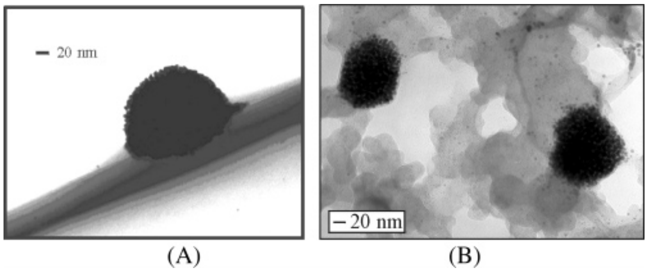

Figure 5. (A) TEM micrograph showing the side view for a spherical assembly from **2**-mediated assemblies of **1**/Au ($r = 100$) without cleaning treatment. The sphere is located on the edge of carbon-coated grid. (**1**/Au = 5.3 ± 1.0 nm). (B) TEM micrograph for a sample obtained from the same assemblies dispersed in carbon black. Carbon black was added 0.5 h after the addition of **2** to **1**/Au. (**1**/Au = 5.3 ± 1.0 nm).

The visibility of individual particles along the periphery of the spherical assembly before the cleaning treatment, in contrast to the poor visibility for those after the cleaning treatment, indicates that the spherical assembly before the treatment was likely softer than that after the treatment. The soft nature was supported by the spreading of the particles at the surface-contact area. In fact, the observation of a semisphere and the presence of a wetting layer surrounding the spherical assembly before the cleaning treatment (Figure 5A) supports the notion that the spherical assembly before the cleaning treatment is relatively soft and has a tendency to partially spread on the substrate surface.

The excess **1** could also have helped the spreading via favorable wetting propensity. A rough estimate shows that the assembly size could be about 20% smaller than what the TEM image showed for the assemblies before the cleaning treatment. After the cleaning treatment, the difference in size determined by TEM from the actual size is likely insignificant because of the decreased softness. These assessments will be examined later by AFM studies of the spherical assemblies cast on flat surfaces.

We believe that the strong interparticle linkage and stability are provided by a combination of the mediation force of **2** and the hydrophobic force of **1**. As an additional piece of evidence to support the strong interparticle interactions, the carbon black was added into the nanoparticle assembly solution to test the viability of breaking the interparticle linkage by the large surface-area carbon surfaces. In a related system in the presence of **1** but in the absence of **2**, we found that aggregates of particles were easily dispersed on the hydrophobic carbon with large surface areas.[28] However, the results for the **2**-mediated assemblies of **1**/Au (Figure 5B) showed that the spherical assemblies remained intact in the presence of carbon. Therefore, the experiment supports our assessment that there exist strong interparticle linkages due to both mediator and template molecules.

1.2. AFM. The spherical assemblies of nanoparticles were further examined using AFM by casting the assembly solution onto a flat substrate such as mica and HOPG. Figure 6 shows a typical set of AFM images for **2**-mediated **1**/Au assemblies of two different sizes on mica substrates. The nanoparticle assemblies were subjected to cleaning treatment before casting.

One important observation is that the spherical assemblies retained their spherical morphology on mica surface. This observation is supported not only by the spherical outlines but also by the height data from the cross-sectional analysis. The average heights of the individual assemblies, 150 nm (A) and 40 nm (B), are largely consistent with TEM data described in the previous section. The nature of the interaction between the spherical assembly and mica must be weak in view of the hydrophilic character of mica surface and the hydrophobic character of **1**/Au nanoparticles and their assemblies. The spherical assembly on mica does not wet the surface and thus retains its shape.

In contrast, the spherical assemblies cast on HOPG revealed a mixture of morphological characters as shown by the different sizes of assemblies and a fluidlike spreading of particles on the surface. This observation is also supported by the cross-sectional height data (Figure 7), which reveal average heights of the surface features, 30 (A) and 10 nm (B), the magnitudes of which are much smaller than those observed for the same nanoparticle assemblies on mica surface (Figure 6). The nature of the interaction between the spherical assembly and HOPG must be relatively strong in view of the hydrophobic character of HOPG surface and the hydrophobic character of **1**-capped Au nanoparticles and their assemblies. The spherical assembly wets HOPG, and thus the particles tend to spread over the surface.

Similar morphological properties have also been observed for spherical assemblies that were not subjected to any cleaning treatment. A set of AFM images for **2** (TE_4)-mediated spherical assemblies of nanoparticles cast on mica and HOPG are shown in Figure 8. On mica (A), the spherical islands with heights of 30−80 nm were observed, reflecting closely the sizes determined by TEM. On HOPG (B), the partial melting over the substrate surface leads to merging between two or three spherical islands. The average height of the monolayer, ∼3.5 nm, closely matches the nanoparticle size.

The unusual partial spreading of nanoparticles over the contacted surface is indicative of the soft nature of the outmost layer around the spherical assembly. This phenomenon could form the basis of a new strategy for manipulating nanoscale linkage between individual assemblies of nanoparticles or nanoscale soldering between small electrode gaps and constructing nanosensor devices.

1.3. SAXS. Small-angle X-ray scattering (SAXS) is a powerful technique for studying structural features of colloidal size materials.[17,25g] We used SAXS to examine our nanoparticle assemblies to gain further understanding of the interparticle spatial properties. The measurement was performed under in-situ condition, that is, during the formation of nanoparticle assembly in the solution. Figure 9 shows a representative set of SAXS data for the **2**-mediated assembly of **1**/Au. For achieving reliable SAXS signals, the nanoparticle concentrations (1.0 μM) were ∼10× higher than the usual concentrations. The r values were, however, kept the same as under the usual condition. The scattered intensity of the samples are plotted versus the q value, with $q \equiv [(4\pi n/\lambda_0)/\sin(\theta/2)]$ being the magnitude of the scattering factor, and n, λ_0, and θ being the refractive index of the vacuum, the wavelength of incident X-ray beam, and the scattering angle, respectively.

---

[28] Maye, M. M.; Luo, J.; Han, L.; Kariuki, N. N.; Zhong, C. J. *Gold Bull.* **2003**, *36*, 75−82.

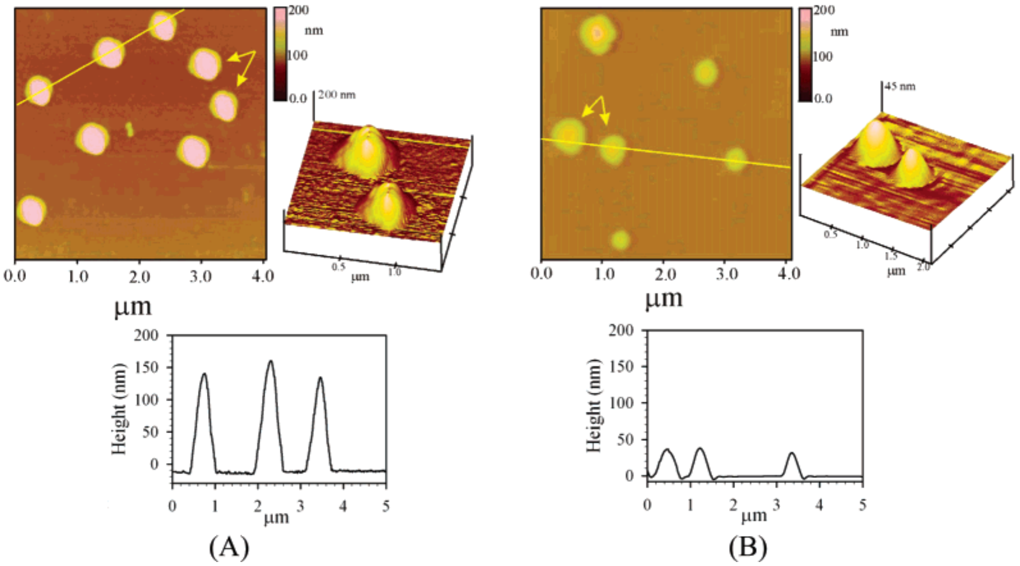

Figure 6. AFM images of **2**-mediated assemblies of **1**/Au (after 1× cleaning treatment) cast on a mica surface. $r = 25$ (A) and 600 (B). A cross-sectional view for the line drawn and a 3D view for the indicated particles are included for each case. (**1**/Au = 5.3 ± 1.0 nm).

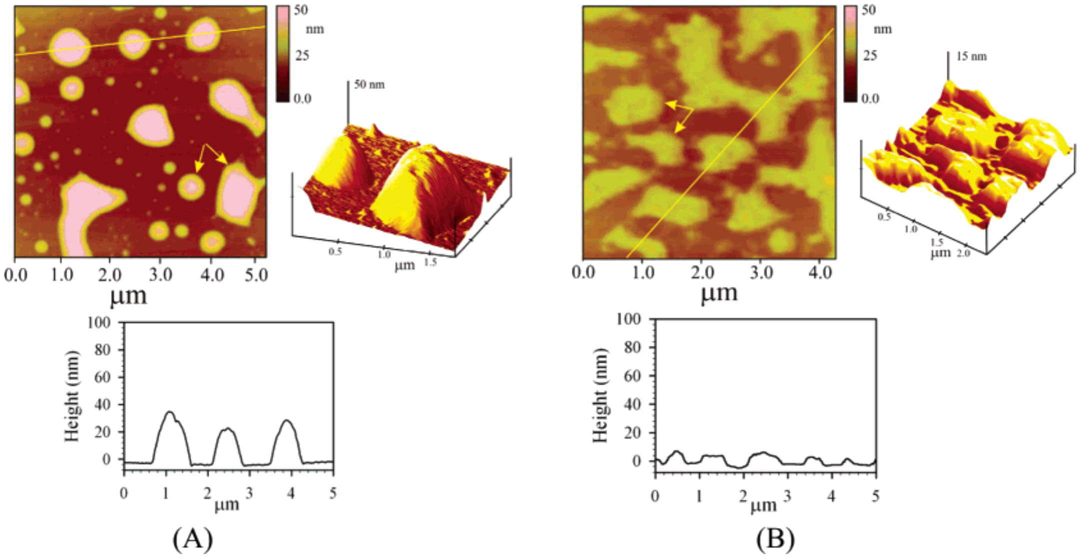

Figure 7. AFM images of **2**-mediated assemblies of **1**/Au (after cleaning treatment) cast on HOPG surface. $r = 25$ (A) and 600 (B). (**1**/Au = 5.3 ± 1.0 nm). A cross-sectional view for the line drawn and a 3D view for the indicated particles are included for each case.

There are two important pieces of information. First, three scattering patterns (a, b, and c) display obvious maxima at $q \approx 0.8\ \mathrm{nm}^{-1}$ ($q_{\max}$). Second, the patterns exhibit an observable shift for $q_{\max}$, which increases with r. The latter reflects the change in interparticle distances. The interparticle center-to-center distances (d) can be derived from the SAXS diffraction patterns, which is expressed in eq 1

$$d = 2\pi/q_{\max} \tag{1}$$

The calculated d_{Au} values are listed in Table 1. On the basis of the average diameter (6.4 ± 0.8 nm) for the **1**/Au used in the SAXS experiment, we obtained an average value of ~2 nm for the interparticle edge-to-edge distance. This value is slightly larger than the length scale expected for the molecule **2** (~0.5 nm) plus two Au−S coordination bonds (~0.5 nm). While the exact origin for this difference will be further probed, we believe that the **2**−**1** combination responsible for the mediator−template assembly played an important role in dictating the overall interparticle distance. The results for pure **1**/Au sample (*d*) showed no $q_{\max}$, suggesting that it is the introduction of **2** which initiated the assembly of nanoparticles.

The subtle decrease of the edge-to-edge distance ($d_{\mathrm{edge-to-edge}}$) with increasing r is suggestive of the dependence of packing density on the assembly size. As the average size of the nanoparticle assemblies increases, the interparticle edge-to-edge distances increases from 1.5 to 2.3 nm. The packing density is actually decreased. On the basis of the SAXS data, the interparticle distance was between the expected molecular lengths of **1** and **2**.

The composition analysis of the nanoparticle assemblies using XPS technique provided another piece of supporting evidence. We analyzed a sample prepared using $r = 300$ and five times of cleaning treatment. We detected the expected elements such as Au (19.1 (±0.4)%), S (0.9 (±0.3)%), C (77.91 (±0.8)%), and Si for the mediator, and N (1.7 (±0.5)%) and Br for the template (Si and Br were detected in separate analyses). On

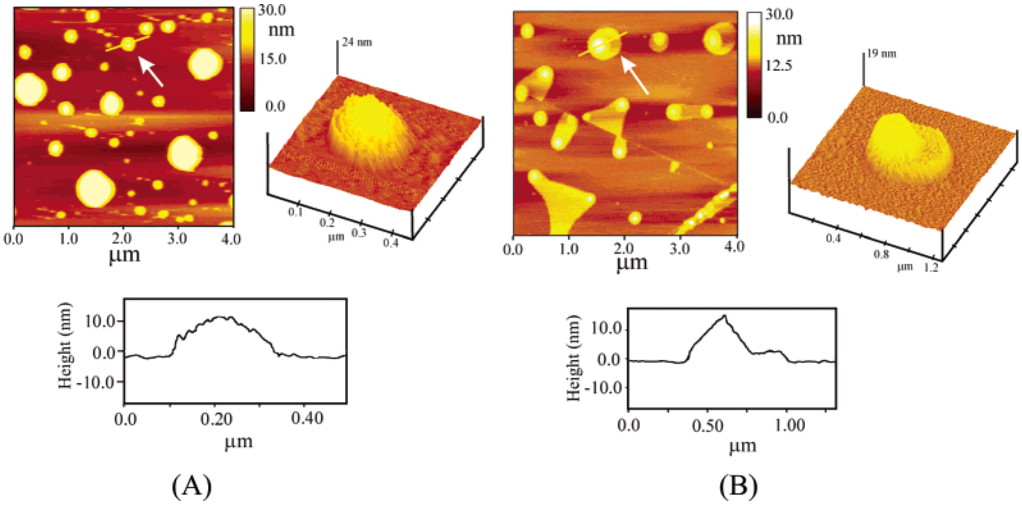

Figure 8. AFM images of **2**-mediated assemblies of **1**/Au cast on mica (A) and HOPG (B). (**1**/Au = 3.7 ± 1.4 nm, **2** = TE_4). A cross-sectional view for the line drawn and a 3D view for the indicated particles are included for each case.

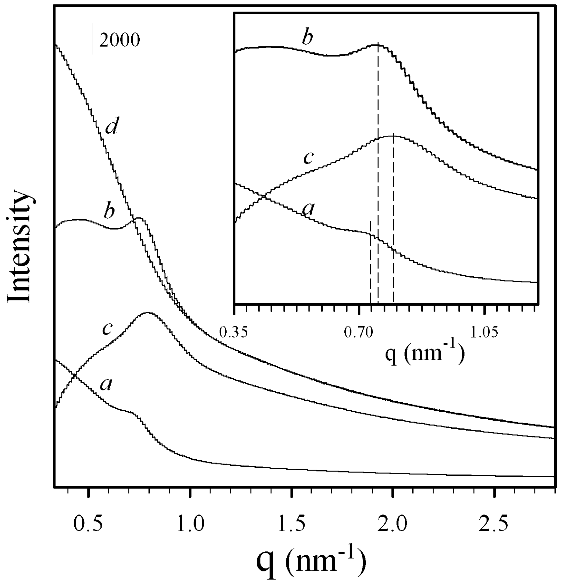

Figure 9. SAXS data for the **2**-mediated assembly of **1**/Au in solutions at three different concentration ratios ($r = 2.5$ (a), 10 (b), and 400 (c)). Curve d is for **1**/Au solution. Insert: a magnified view of the peak region. (**1**/Au = 6.4 ± 0.8 nm).

Table 1. SAXS Data and Corresponding Interparticle Distances[a]

r	q (nm^{-1})	d ($d = 2\pi/q$)	$d_{\text{edge-to-edge}}$
0			
2.5	0.72	8.7 nm	2.3 nm
10	0.74	8.4 nm	2.0 nm
400	0.79	7.9 nm	1.5 nm

[a] (**1**/Au: 6.4 ± 0.8 nm).

the basis of the average N% and S% detected, the value 1.85 was obtained for the relative N-to-S ratio, which translates to approximately six molecules of **1** for every molecule of **2**. In comparison, a feeding ratio (r) of 300 for the nanoparticle assembly would translate to approximately one **1** for every two **2**. The difference of these two relative ratios is indicative of the thermodynamic competition of the template and the mediator molecules responsible in the nanoparticle assembly. The predominance of **1** in the assembly is consistent with the conclusion of our recent study of the reaction enthalpy, which is quite close to the cohesive energy of hydrocarbons via van der Waals interactions.

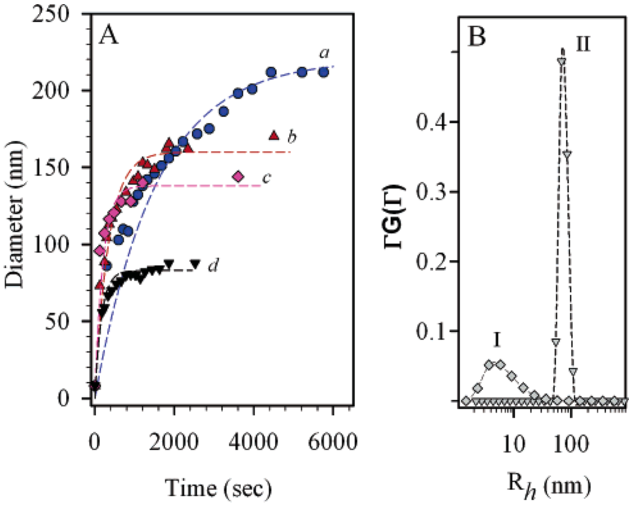

Figure 10. (A) DLS data for the evolution of spherical size as a function of time for a series of **2** concentrations: ([**1**/Au] = 0.0072 μM and [**2**] = 0.16 (● (a, blue)), 0.32 (▲ (b, red)) 1.25 (♦ (c, pink)), 25.0 μM (▼ (d, black)). The data are fitted with $d = d_0[1 - \exp[-(kt)^n]$. (B) A plot of $\Gamma G(\Gamma)$ versus R_h from CONTIN analysis for the isolated (I) and the assembled **1**/Au (II) at [**2**] =0.16 μM. (**1**/Au = 5.1 ± 0.9 nm). Curve II in B is for data corresponding to curve a (~2400 s) in A.

2. Optical Properties. The nanoparticle assemblies displayed interesting optical properties that are highly responsive to changes in assembly size, chemical environment, and molecular structures. Such responsive optical properties could find applications in areas such as sensors and biosensors. This section entails the characterizations of the optical properties using dynamic light scattering and absorption spectrophotometric techniques.

2.1. Light Scattering and Optical Absorption in Response to Assembly Size Evolution. Figure 10 shows a representative set of DLS data obtained for **2**-mediated assembly of **1**/Au. The diameter of the spherical assembly is plotted against time at four different concentrations of **2**. This set of data provides dynamic information on the controlled growth of spherical assemblies in the solution. The size was determined from the

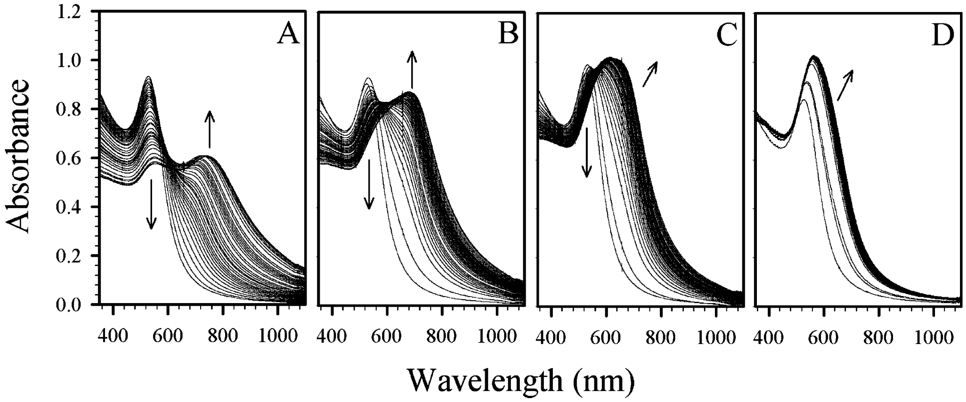

Figure 11. UV−vis spectral evolution for the **2**-mediated assembly of **1**/Au ([**1**/Au] = 0.1 μM,) with different *r* of 1 (A), 50 (B), 100 (C), 600 (D). (**1**/Au = 5.1 ± 0.9 nm). The spectral evolutions were recorded within the time frame of 30 min, and the arrows shown in the graphs indicate the directions of the spectral evolution versus time.

hydrodynamic radii of the assemblies on the basis of CONTIN analysis of the characteristic line width (Γ).[27,29]

There are three important findings here. First, the trend for the increase in the assembly size (*D*) with time can be fitted to a modified model of crystallization and growth[16c] where the critical growth exponent is close to 1. This finding is indicative of lower growth dimensionality, consistent with the spherical shape. Second, the final size of the nanoparticle assemblies increases with decreasing concentration of the mediator, which is consistent with TEM and UV−vis data. Finally, the spherical assemblies are highly monodispersed, as evidenced by the sharpness of the peak in the plot of $\Gamma G(\Gamma)$ versus R_h (e.g., Figure 10B). DLS was previously utilized to monitor the assembly of gold nanoparticles in the presence of DNA.[30]

In contrast to the light scattering, the optical absorption of Au nanoparticles and assemblies is associated with the surface plasmon (SP) resonance band. The origin of the SP band is the coherent excitation of free conduction electrons because of polarization of the electrons induced by the electrical field of incident light.[31,32] A change in absorbance or wavelength of the SP band provides a measure of particle size, shape, and aggregation or elongation properties. Figure 11 shows a typical set of spectra for the evolution of the SP band in response to the addition of **2** to a solution of **1**/Au ([**1**/Au] =0.1 μM) under different values of *r* (25 (A), 50 (B), 100 (C), and 600 (D)).

The gradual spectral evolution of the SP band is accompanied by color change of the nanoparticle solution from red to purple or blue. The spectral envelope of the SP band apparently consists of two overlapping bands. At the lower concentration of **2**, these two bands are clearly resolved at 520 and 780 nm. The display of the isosbestic point at 560 nm is indicative of the involvement of two major species (i.e., Au nanoparticles and nanoparticle assemblies) in the reaction solution. In comparison with the SP band at 520 nm observed for **1**/Au, the extent of this red shift is inversely related to the concentration of **2**, as evidenced by the shift from 580 to 780 nm with the decrease of *r*. The ratio of ~600 translates to an excess of **2** for a full monolayer encapsulation on the 5-nm Au core. The ratio of ~1 corresponds to ~1 molecule of **2** per nanoparticle. The nanoparticle assemblies derived from low concentrations of **2** (e.g., Figure 3C) eventually precipitated after 1−2 days, whereas those obtained from higher concentrations (e.g., Figure 1A) remained soluble for weeks. The average diameter of the spherical assemblies, as determined by TEM, is linearly related to the wavelength of the SP band associated with the nanoparticle assemblies. The DLS data has already revealed that the average diameter decreases with increasing *r*. Therefore, there is correlation between the change in morphological properties and the change in SP optical properties.

2.2. Light Scattering and Optical Absorption in Response to Nanoparticle Disassembly. Both DLS and UV−vis data exhibited remarkable responses to the disassembly of **2**−**1**/Au assemblies upon addition of molecules with a stronger affinity to gold than **2** or **1**. Decanethiol (**3**) was used as such a molecule that can replace the ligand capped on nanoparticles or assemblies via exchange reaction (e.g., **2**, **1**). This process involved the replacement of **2** bound to Au by **3** and was dependent on the relative concentrations of **3**, **2**, and **1**/Au. Thiols exhibit higher binding affinity to gold than thioethers. Figure 12A shows a typical set of DLS data illustrating the change of light scattering in the assembly/disassembly processes. Indeed, the increasing trend for the assembly size was reversed by the addition of thiol. A TEM micrograph from a sample taken during the disassembly process is included to illustrate the presence of individual nanoparticles along the peripheral areas of the spherical assembly as a result of the disassembly.

Similar responses have also been observed for the absorbance of the SP bands associated with the individual nanoparticles (520 nm) and the nanoparticle assemblies (650 nm). Figure 12B shows a typical set of absorption data of SP band at both 520 and 650 nm to illustrate their responses to the disassembly process. In Figure 12B, **3** was added after both SP bands reached a constant value. The reversal of the SP absorption for these assemblies upon addition of **3** to the reaction solution is evident for both SP bands. This finding is significant because it suggests that the nanoparticles in the spherical assembly are held together by relatively weak interactions and can be disassembled into individual nanoparticles by **3**.

When a relatively low concentration of **3** ([**2**] ≈ [**3**]) was added into the assembling solution during its early stage, for

---

(29) (a) Liu, T.; Diemann, E.; Li, H. L.; Dress, A. W. M.; Muller, A. *Nature* **2003**, *426*, 59−62. (b) Provencher, S. W. *Comput. Phys. Commun.* **1982**, *27*, 229−242.

(30) (a) Storhoff, J. J.; Lazarides, A. A.; Mucic, R. C.; Mirkin, C. A.; Letsinger, R. L.; Schatz, G. C. *J. Am. Chem. Soc.* **2000**, *122*, 4640−4650.

(31) (a) Link, S.; El-Sayed, M. A. *Int. Rev. Phys. Chem.* **2000**, *19*, 409−453. (b) Papavassiliou, G. C. *Prog. Solid State Chem.* **1979**, *12*, 185−271.

(32) Ung, T.; Liz-Marzan, L.; Mulvaney, P. *J. Phys. Chem. B* **2001**, *105*, 3441−3452.

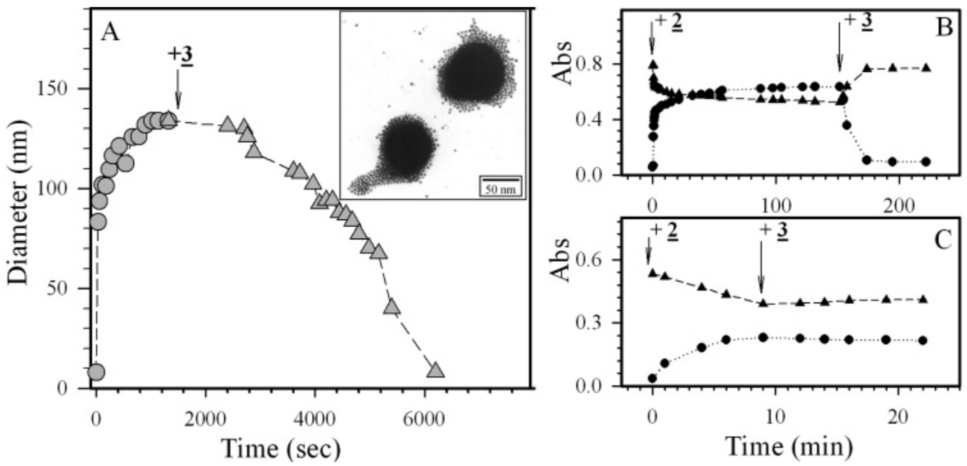

Figure 12. Optical data showing the assembly and the disassembly upon addition of **2** or **3** (**3**: decanethiol) into the solution. (A) DLS data showing the assembly upon addition of **2** at $r = 25$ (●), and the disassembly upon addition of **3** ([**3**] = 10 μM) (▲). Insert: TEM micrograph for a sample taken during the disassembly process. (B and C) Temporal dependence of SP band absorbance at 520 nm (▲) and 780 nm (●) for a solution of **1**/Au (0.1 μM) upon addition of **2** followed by addition of **3** (6 μM (B) and ~1 μM (C)). (**1**/Au = 5.1 ± 0.9 nm).

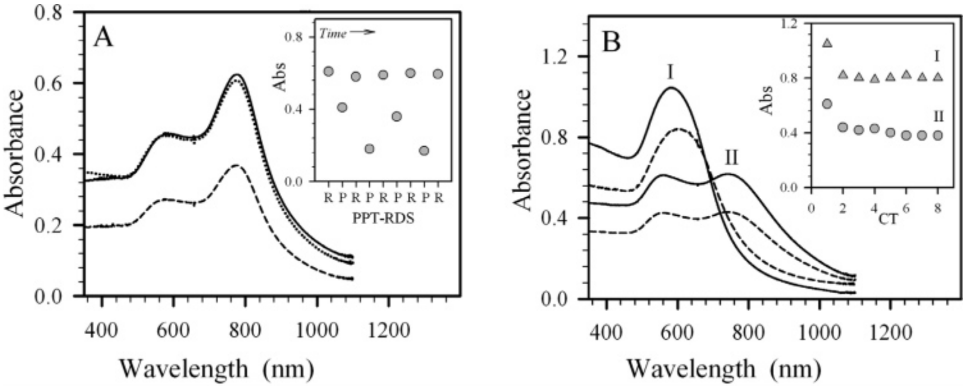

Figure 13. UV−vis spectra for **2**-mediated assembly of **1**/Au in response to PPT−RDS cycles (A) and CT cycles (B). (A) A sample obtained from $r \approx 25$; solid line: before precipitation; dashed line: the solution after partial precipitation; dotted line: the redispersed solution. Insert: the absorbance at 760 nm in the PPT−PDS cycles (R: redispersed assemblies; P: the solution after partial precipitation for ~6, ~15, ~8, and ~6 h). (B) Samples obtained at $r \approx 10$ (I) and ≈ 600 (II). Solid line: before precipitation; dashed line: the redispersed assemblies after the first CT. Insert: the absorbance at 590 and 790 nm vs CT cycles. (**1**/Au = 5.3 ± 1.0 nm).

example, ~10 min, the change of the absorbance was clearly leveled off to a relatively constant value, suggesting that the assembly process was effectively stopped (Figure 12C). In this case, the small-sized spherical assemblies were essentially converted to **3**-capped spherical assemblies of **2**−**1**/Au, so that no further growth of the assembly can occur. Such assemblies were in fact stable for days. This finding is intriguing because it demonstrates the viability of regulating the size of the spherical assemblies by a third capping component.

2.3. Optical Absorption in Response to Precipitation−Dispersion Cycle. Since the spherical assemblies undergo changes both in size and packing density during the precipitation−redispersion treatment, we further examined its effect on the SP band. Figure 13A shows the changes of the SP bands in response to the precipitation−redispersion cycle (PPT−RDS). While each precipitation process led to a decrease of the absorbance (dashed), each redispersion brought the absorbance back (dotted) with an insignificant change in spectral characteristic. In terms of spectral shape and absorbance, no significant change was observed even after multiple precipitation−dispersion cycles.

The excess of **1** (~31 mM) in the solution of nanoparticle assemblies can be removed via precipitation or centrifugation through which the **1**-containing Tl layer is discarded and fresh Tl was added. Such cleaning treatment (CT) can undergo many dispersion−redispersion cycles in fresh solvent which not only purifies effectively the assemblies but also allows processing of the assemblies without significant destruction. Figure 13B shows a set of spectral data for a solution of **2**−**1**/Au after multiple CT cycles. Indeed, the spectral characteristics showed little change in response to the cycle. After an initial ~20% change, the absorbance value also exhibited little change after at least eight cycles. Clearly, the nanoparticle assemblies were stable in the absence of **1** in the solution.

To better understand the correlation of the optical properties with size and interparticle spatial properties of the nanoparticle assembly, the spectral simulation was performed based on Mie theory.[31,32] In Mie theory (eq 2),[31]

$$\frac{\gamma}{NV} = \frac{18\pi {\epsilon_\alpha}^{3/2}}{\lambda} \times \frac{\epsilon_2}{(\epsilon_1 + 2\epsilon_\alpha)^2 + {\epsilon_2}^2} \tag{2}$$

the extinction coefficient γ is related to volume concentration of the particles (NV, N: the number of spheres per unit volume; V: the volume of each sphere) for nanoparticles or the assembled nanoparticles, which is inversely proportional to the

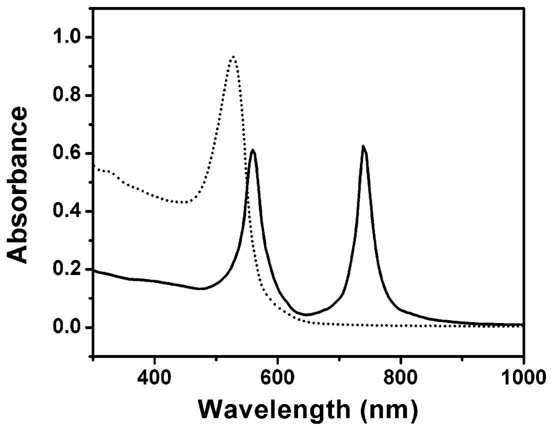

Figure 14. The SP bands simulated on the basis of Mie theory for Au nanoparticles (dotted line) and spherical assemblies (solid line).

Table 2. Simulation Results for the SP Bands

	based on Mie theory				based on modified Mie theory[a]			
	SP (Au_{nm})		SP (TE_3–Au_{nm})		SP (Au_{nm})		SP(TE_3–Au_{nm})	
system	NV[b]	ϵ_α	NV[b]	ϵ_α	d[b]	ϵ_α	d[b]	ϵ_α
Au_{nm}	7.6	2.0			60	1.8		
TE_3-Au_{nm}	1.6	3.5	0.3	10.2	10.1	3.3	0.3	10.1
TE_3-Au_{nm}[c]	1.1	3.5	0.2	10.2	7.5	3.3	0.3	10.2

[a] ϕ remains largely constant. [b] In arbitrary unit. [c] After cleaning treatment.

edge-to-edge distance ($d_{edge-to-edge}$) of nanoparticles in the spherical assembly, and the dielectric medium constant (ϵ_α). ϵ_1 and ϵ_2 are the real and complex part of Au, and λ is thewavelength of light in a vacuum in eq 2. In a modified Mie theory (eq 3),[32]

$$T_{film} = \frac{(1-R)^2 + 4R\sin^2\psi}{R^2\exp(-\alpha d) + \exp(\alpha d) - 2R\cos(\zeta + 2\psi)} \quad (3)$$

R is the reflectance at normal incidence which is related to the effective dielectric function (ϵ_{av}) for the metal nanoparticles. The variates α, ψ, and ζ are related to ϵ_{av}, thickness of the nanoparticle ensemble (d), and λ. ϵ_{av} is related to the ϵ_1, ϵ_2, ϵ_α, and the volume fraction of the particles (ϕ). Briefly, the light transmission T_{film} is related to ϕ, d, and ϵ_α. The theoretical analysis of the SP band data was recently shown to provide useful insights into the interparticle properties.[33] Figure 14 shows the spectral simulation based on the spectrophotometric data of SP bands shown in Figure 13B(II). In general, the band position and absorbance can be simulated well, but the simulated bandwidth is usually narrower than the experimental data. Similar results have also been obtained using the modified Mie theory. The simulation results are shown in Table 2.

The simulation results are quite consistent with both modified and unmodified Mie theories in terms of the general trend of the parameters. The dielectric medium constant is increased by a factor of ~5 from individual nanoparticles to spherical assemblies. This increase reflects the difference in interparticle dielectric medium properties between Au and **2**−**1**/Au. The interparticle structure for the latter consists of both mediator and template molecules in close distances, which is expected to exhibit a higher dielectric medium constant. In addition, the decrease in the volume concentration (*NV*) or thickness of the nanoparticle ensemble (d) likely reflects the changes of interparticle spacing, intersphere spacing, and size of the spherical assemblies. The assessment of the relative contributions of these parameters is part of our ongoing investigation.

Conclusions

In conclusion, we have shown that the mediator−template strategy is an effective route for the assembly of nanoparticles into size-controllable spheres. While this strategy is demonstrated for multidentate thioether-mediated assembly of tetraoctylammonium-capped gold nanoparticles, its utility is entirely general for the assembly of nanoparticles in a variety of systems, depending on the chemical or structural nature of the mediators and templates. The high monodispersity of the spherical assemblies and the viability of forming ordered morphologies are unprecedented. The subtle decrease of interparticle distance with increasing the assembly size is suggestive of the dependence of the packing density on the assembly size and the mediator−template interaction. The spherical assemblies can be processed effectively by precipitation and redispersion leading to improved monodispersity and higher packing density. The interparticle linkage and stability are provided by a combination of the mediation force of the multidentate thioether and the hydrophobic force of the tetraalkylammonium bromide template. The discovery of the soft−hard nature of the nanoparticle assemblies and their interactions with contacting substrates could form the basis of a new strategy for manipulating nanoscale linkages between nanoparticles assemblies, soldering nanoelectronics, and constructing nanosensor devices.

The findings of the responsive optical properties of the nanoparticle assemblies to several chemical, morphological, and structural parameters in assembly, disassembly, sizing, and interparticle spacing may open new opportunities for both fundamental and practical explorations. The light scattering and surface plasmon resonance absorption are important for assessing the size-controllability, the interparticle spatial properties, and the interparticle interactions in the assembly/disassembly processes. The discovery of the disassembly into individual nanoparticles and the size regulation by a third capping component could form the basis for applications in controlled drug delivery. Furthermore, the experimental and theoretical correlations of the morphological and optical properties support the fundamental basis for the mediator−template strategy as a general and versatile assembly technique.

Acknowledgment. This work is supported by the National Science Foundation (CHE-0349040) and the 3M Corporation. M. M. M. thanks the Department of Defense for a National Defense Science & Engineering Graduate Fellowship sponsored by ARO. D. R. also thanks Research Corporation for a Cottrell College Science Award. We thank Mr. Mark Engelhard for help in XPS analysis.

JA044408Y

---

(33) Luo, J.; Maye, M. M.; Han, L.; Kariuki, N. N.; Jones, V. W.; Lin, Y.; Engelhard, M. H.; Zhong, C. J. *Langmuir* **2004**, *10*, 4254−4260.